Applied Water Science (2024) 14:141
https://doi.org/10.1007/s13201-024-02194-3

ORIGINAL ARTICLE

Sustainable fabrication of a novel ZIF-67 modified with *Atriplex halimus*-mediated MoO_3/GO-NH_2 for expeditious removal of nitrophenol

Ahmed S. Elbay[1,2] · Manal Fawzy[1,2,3] · Eman M. Abd El-Monaem[4] · Abdelazeem S. Eltaweil[4,5]

Received: 8 January 2024 / Accepted: 16 April 2024 / Published online: 21 May 2024
© The Author(s) 2024

Abstract

Herein, a novel, green, and sustainable MoO_3/ZIF-67/AmGO composite has been fabricated for the removal of notorious o-nitrophenols (*o*-NPs) from wastewater. *Atriplex halimus* L. (saltbush) served a dual function where the plant extract was used for the synthesis of molybdenum trioxide (MoO_3) NPs, while the spent biomass-derived biochar was utilized as feedstock to produce green graphene oxide (GO). Ultimately, the MoO_3/ZIF-67/AmGO composite was in situ fabricated by mixing MoO_3 and AmGO with ZIF-67 during its preparation by the self-templating approach. Remarkably, the adsorption of *o*-NP onto MoO_3/ZIF-67/AmGO attained equilibrium in just less than 10 min. The kinetics and isotherms analyses verified that the *o*-NP adsorption onto MoO_3/ZIF-67/AmGO adhered to the Pseudo-2nd-order and Freundlich models, with a consistent q_{max} value of 500 mg/g. A conceivable adsorption mechanism was investigated in detail. Moreover, the ionic strength test implied the impact of the salting-out phenomenon in boosting *o*-NP adsorption. The eco-friendly MoO_3/ZIF-67/AmGO proves to be a sustainable adsorbent, displaying excellent recyclability in consistently removing *o*-NP across multiple cycles.

Keywords Atriplex halimus · MoO_3 · AmGO · ZIF-67 · o-NP

Introduction

Indubitably, water pollution is a major environmental concern that should be scrutinized since anthropogenic activities release a variety of contaminants, such as heavy metals, dyes, aromatic compounds, and fertilizers (El-Subruiti et al. 2019; Rafi et al. 2018). Aromatic compounds, especially phenolic compounds, are vastly employed in bountiful industrial processes, including plastics, pigments, pesticides, petroleum industries, etc. (Koubaissy et al. 2011). Nonetheless, the accumulation of these phenolic compounds in water causes deleterious health concerns for humans, animals, and aquatic life since they are mutagenic and carcinogenic. Hence, the World Health Organization specifies a maximum allowable level of phenol in drinking water of 2 mg/L (Tabana et al. 2020).

Nitrophenols are phenolic compounds that are drained during processing in several industries, comprising medicines, dyes, explosives, and herbicides. Nitrophenols such as *o*-NP suffer limited degradability and high solubility in water; therefore, *o*-NP exists with over concentrations in the contaminated water bodies by industrial wastes. Besides, *o*-NP can cause significant odor and taste issues in water

✉ Ahmed S. Elbay
Ahmed.Elbay@alexu.edu.eg

Manal Fawzy
dm_fawzy@yahoo.com

Eman M. Abd El-Monaem
emanabdelmonaem5925@yahoo.com

Abdelazeem S. Eltaweil
abdelazeemeltaweil@alexu.edu.eg

1 Environmental Sciences Department, Faculty of Science, Alexandria University, Alexandria 21511, Egypt

2 Green Technology Group, Faculty of Science, Alexandria University, Alexandria 21511, Egypt

3 National Egyptian Biotechnology Experts Network, National Egyptian Academy for Scientific Research and Technology, Cairo, Egypt

4 Department of Chemistry, Faculty of Science, Alexandria University, Alexandria 21321, Egypt

5 Department of Engineering, Faculty of Technology and Engineering, University of Technology Applied Sciences, Al Masnaah, Sultanate of Oman

and constitute a risk to people even at low doses (Aazza et al. 2017). There are various methods for facing the actual jeopardy of *o*-NP, including the Fenton process, membrane filtering, electrochemical approaches, biodegradation, and adsorption (Abd El-Monaem et al. 2023a, b, c). Noteworthy, adsorption is still the most convenient strategy for remedying wastewater from prejudicial industrial wastes, with outstanding benefits comprising, low capital cost, availability, facile operation, and energy saving (Demirbas 2008). Nevertheless, the adsorption technique suffers the main bottleneck since it does not eliminate contaminants, rather, it transports them from wastewater to the adsorbent surface (Bestawy et al. 2020; Qin et al. 2023b). Hence, myriad sorts of adsorbents have continuously evolved to outdo the jeopardy of the notorious *o*-NP, such as biochar (Pauletto et al. 2021), graphene derivatives (Severo et al. 2023), zeolites (Pham et al. 2016), metal oxide nanoparticles (Aazza et al. 2017), layered double hydroxide (Sellaoui et al. 2021) and metal–organic frameworks (MOFs) (Chen et al. 2017). Since the preceding adsorbents require a long adsorption period to attain equilibrium, they raise the cost of the adsorption process and limit their large-scale applicability. Therefore, it is necessary to develop highly efficient, eco-friendly, and sustainable *o*-NP adsorbents.

Zeolitic imidazolate frameworks (ZIFs), a subtype of metal–organic frameworks (MOFs), are built from coordinated transition metal ions with organic imidazole and have analogous structures to zeolites. However, the ZIFs configuration contains imidazole substitute oxygen instead of silicon in the case of zeolite. Interestingly, ZIFs are distinguished with propitious properties, including extraordinary mechanical stability, ultrahigh chemical stability owing to metal-nitrogen bonding, and variable pore size and surface area (Cheng et al. 2018). Specifically, ZIF-67 is a shining member of the ZIFs family, where it is prepared at a low cost, easy way using the self-templating method, in addition to its excellent adsorbent (Cui et al. 2019).

Metal oxide nanoparticles have lately acquired notable attention because they are low-cost and efficient adsorbents for wastewater remediation. Metal oxides exhibit distinctive physicochemical features like customizable form and size, plentiful surface-active sites, and chemically stable (Wang et al. 2020). Additionally, metal oxides contain diverse functional properties depending on their composition, crystal structure, shape, doping, inherent defects, etc. Metal oxides are composed of varied shapes like particles, tubes, and sheets (Ghosh et al. 2022). Numerous chemical and physical approaches have been used for fabricating nanoparticles, however, these methods are costly, energy-intensive, and harmful to the environment (Hanlon et al. 2014; Masjedi-Arani et al. 2020; Wang et al. 2018; Yadav et al. 2012). On the other hand, the biosynthetic strategy, in particular using plant extract is a rapid, safe, eco*o*-friendly, and inexpensive way to fabricate nanoparticles owes to the presence of numerous photoactive ingredients in plant extracts that function as both reducing and stabilizing agents (Hosny et al. 2022). One of these notable metal oxide nanoparticles is molybdenum trioxide nanoparticles, which possess three different types: hexagonal (h-MoO_3), orthorhombic (α-MoO_3), and monoclinic (β-MoO_3). Among them, the stable and ecologically safe (α-MoO_3) has found widespread use in various applications such as adsorption, sensors, lithium-ion batteries, catalysis, and solar cells (Hasan et al. 2021).

Significant global research has resulted in the development of new carbon materials that have been successfully utilized in varied practical applications, comprising biosensors, drug delivery, and wastewater treatment (Patel et al. 2019). Because of the individual structural dimensions and exceptional mechanical, thermal, electrical, chemical, and optical properties of carbon materials, they are deemed the most adaptable materials for enhancing wastewater treatment processes. The most investigated carbon-based nanomaterials include carbon nanotubes, fullerenes, quantum dots, and graphene derivatives such as graphene oxide (Piaskowski and Zarzycki 2020). In recent years, graphene oxide (GO) has exhibited significant advances in wide-ranging applications, including catalysis, drug delivery, and sensors. In addition, GO has shown particular interest in wastewater purification owing to its large specific surface area, high adsorption capacity, and high level of mobility in solution (Dayana Priyadharshini et al. 2022). Notably, the amine group endows GO's superior adsorption aptitude in removing pollution from contaminated water (Huang et al. 2020). Although plant-based GO was reported frequently by many researchers (Abdelfatah et al. 2022; El-Maghrabi et al. 2021; Mahmoud et al. 2022a, b; Mahmoud et al. 2022a, b), no published data are available for the green synthesizes of AmGO. However, the use of plant biomass for the manufacturing of AmGO is an environment-friendly, cost-effective, and sustainable route.

In this context, our study intended to fabricate MoO_3/ZIF-67/AmGO composite, from renewable and sustainable resources, for removing *o*-NP from aqueous media. It is noteworthy to mention that a lignin-rich *Atriplex halimus* plant was used for the first time to fabricate GO and MoO_3. For the sake of having an extra amount of amino group, GO was aminated using ethylene diamine. Then, the green-synthesized MoO_3 and AmGO were mixed with the metal/ligand solution during the preparation of ZIF-67 via the green self-templating tactic. Thus, in situ fabricate the MoO_3/ZIF-67/AmGO composite. After performing a complete characterization study of MoO_3/ZIF-67/AmGO, its adsorption efficacy was scrutinized in removing the persistent *o*-NP from an aqueous medium. Moreover, the in-depth adsorption mechanism to the MoO_3/ZIF-67/AmGO/*o*-NP system was proposed based on kinetic, thermodynamic, and

isothermic studies; in addition, XPS analysis of the *o*-NP-loaded MoO_3/ZIF-67/AmGO. Importantly, to confirm the viability of the green MoO_3/ZIF-67/AmGO composite, ionic strength, and recyclability tests were executed.

Experimental part

Materials

Text S1 compiles the chemicals used in the preparation of MoO_3/ZIF-67/AmGO composite.

Preparation of the *Atriplex halimus* extract

Atriplex halimus L. is a trifoliate perennial halophytic plant that survives harsh drought and salinity conditions. The extensive natural habitat of *A. halimus* spans Eurasia, the Middle East, and the Mediterranean basin (Walker and Lutts 2014). *A. halimus* specimens were collected from their natural habitat in the Mediterranean coastal land of Egypt. *A. halimus* was cleaned, with deionized water, dried in the open air then placed in the oven at 60 °C till completely dried. Next, the dried plants were pulverized into a fine powder. About 5 g of the granulated plants was dipped into 100 mL distilled water and kept for 1 h at 80 °C. Eventually, the plant's extract was allowed to cool and then filtered using filter paper.

Preparation of MoO_3 nanoparticles

The fabrication of MoO_3 proceeded by co-precipitation approach as follows; 0.01 M of aqueous $(NH_4)_6Mo_7O_{24}{\cdot}4H_2O$ solution was slowly dropped into 50 mL of plant extract. The pH of the Mo-precursor/plant extract solution was adjusted to 10 using NaOH. Next, the suspended particles were stirred for 2 h, purified with deionized H_2O and ethanol, and dried at 75 °C overnight. Eventually, the formed powder was pyrolyzed for 2 h at 600 °C.

Preparation of AmGO

Firstly, BC was fabricated by calcinating 10 g of *A. halimus* powder at 350 °C for 45 min in a muffle furnace. Secondly, the green GO was synthesized via the Hummer process with some modifications (Abdelfatah et al. 2022). In 100 mL of concentrated H_2SO_4, 2 g of *A. halimus*-based BC and 1 g of $NaNO_3$ under stirring at 5 °C. After adding 10 g $KMnO_4$, the reactants mixture was retained under stirring for another 1 h. Next, the reaction temperature was elevated to 40 °C with continual stirring for 30 min. Then, 100 mL of deionized water was added to the reaction container, increasing its temperature to 90 °C for 2 h. To finish the reaction, 280 mL of deionized water followed by 30 mL of H_2O_2 were dipped into the reaction mixture. The brown product was allowed to settle overnight before being washed three times with HCl (10%) and distilled water and drying overnight at 50 °C.

The amination of GO was performed based on the authors' previous method (Omer et al. 2022). 0.3 g of GO was diffused in 30 mL deionized water (solution A), and 0.2 mL EDA was added to 30 mL ethanol (solution B). Next, solutions A and B were combined, and the resulting solution was gently stirred for 24 h. After that, the product was centrifuged, washed with ethanol, and dried in an oven at 60 °C for 6 h.

Preparation of MoO_3/ZIF-67/AmGO composite

MoO_3/ZIF-67/AmGO was in-situ fabricated as follows; 0.1 g of AmGO was sonicated in 125 mL methanol for 30 min, then 0.2 g of MoO_3 was mixed under vigorous stirring. After 30 min, 2.12 g $Co(NO_3)_2{\cdot}6H_2O$, and 2.54 g (MeIm) were dipped into the AmGO/MoO_3 mixture and stirred for 24 h. Ultimately, MoO_3/ZIF-67/AmGO was rinsed twice with methanol and kept overnight in an oven at 60°C. Notably, ZIF-67 was typically prepared by the former procedure, except the step involves adding AmGO and MoO_3.

The green-fabricated MoO_3/ZIF-67/AmGO composite and its authentic components were characterized by various techniques, as explained in the supplementary Text S2.

Batch adsorption

Series adsorption tests proceeded to pick out the finest conditions for the *o*-NP adsorption onto MoO_3/ZIF-67/AmGO composite. The pH influence was scrutinized in a pH range between 3 and 11. The leverage of the MoO_3/ZIF-67/AmGO dosage (0.005–0.02 g) was examined to choose the appropriate dose based on the environment and economic requirements. In addition, the impact of the process temperature on the *o*-NP removal aptitude was investigated at varied temperatures (25–55 °C). The effect of *o*-NP initial concentration on the removal ability of composite has been tested at a concentration range from 50 to 300 mg/L. The influence of the initial *o*-NP concentrations (50–200 mg/L) was studied. The remaining concentration of *o*-NP in the bulk solution was determined spectrophotometrically at 344 nm, then the adsorption aptitude (Eq. 1) and removal% (Eq. 2) were reckoned.

$$q_t = \frac{(C_0 - C_t) \times V}{m} \tag{1}$$

$$R\% = \frac{C_0 - C_t}{C_0} \times 100 \tag{2}$$

The C_o symbol represents the initial *o*-NP concentration, while the final concentration denotes C_t. The MoO_3/ZIF-67/AmGO dosage is m, and the *o*-NP volume is V.

Ionic strength test

The ionic strength influence on the aptitude of *o*-NP adsorption was evaluated at a NaCl concentration range of 0.2–1 mol/L. A certain weight of NaCl was mixed with the aqueous *o*-NP solution at a neutral pH, then the composite was added. After five min, a specimen was drawn to assess the concentration of unabsorbed *o*-NP.

Reusability test

To examine the durability of MoO_3/ZIF-67/AmGO, a five-cycle regeneration test was performed in which the composite was separated from *o*-NP with neutral pH (pH 7) after five minutes, washed in 25 mL of 1M NaOH followed by water for *o*-NP desorption, and reused in the following cycle.

Results and discussion

Characterization of MoO_3/ZIF-67/AmGO

The fabrication of the MoO_3/ZIF-67/AmGO composite, as illustrated in Fig. 1, was divided into two consecutive steps. Firstly, after sonicating AmGO to increase dispersion, green synthesized MoO_3-NPs were added. MoO_3-NPs interacted with OH and NH_2 presented in AmGO. Subsequently, ZIF-67 precursors were added to the MoO_3-NPs/AmGO mixture and stirred for 24 h, resulting in the formation of ZIF-67 crystals on the AmGO surface. Cobalt ions in ZIF-67 and oxygen and nitrogen atoms in AmGO are bound together via a coordination bond. Furthermore, there is a π-π stacking

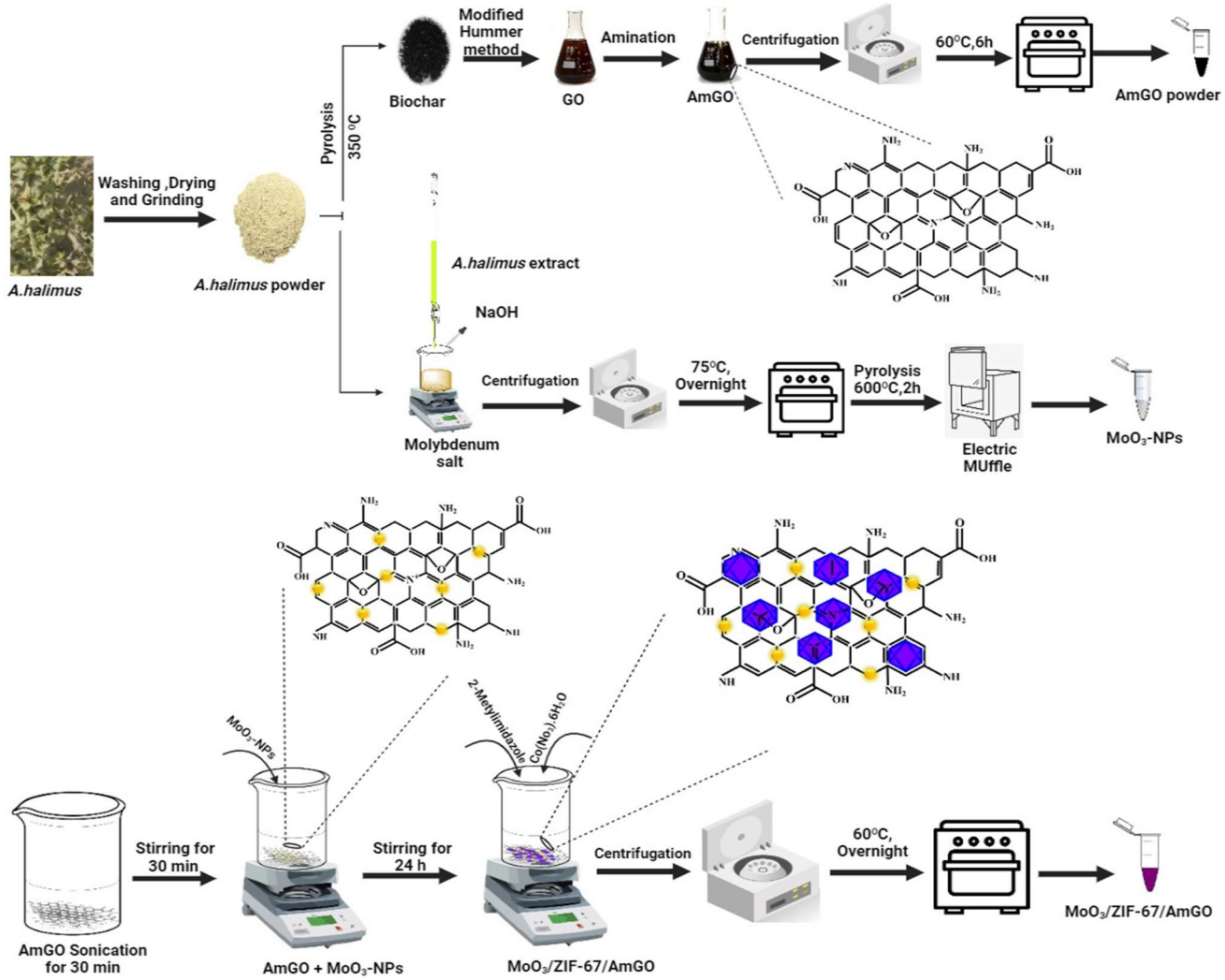

Fig. 1 Preparation scheme for the fabrication of MoO_3/ZIF-67/AmGO composite

interaction between the aromatic imidazole rings of ZIF-67 and the π-electrons of the AmGO's aromatic rings.

FTIR

For identifying functional groups in the green-fabricated MoO_3/ZIF67/AmGO, the composite, and its authentic components were analyzed via FTIR (Fig. 2A). The GO spectrum clarified the related bands to epoxy, C–O, C=O, and C–OH at wave numbers 1044, 1625, 1724, and1372 cm^{-1}, respectively (Abd El-Monaem et al. 2023a, b, c). The AmGO spectrum denoted the successful amination of GO, where the belonging bands to C–N and N–H emerged at 1450 and 1520 cm^{-1}. Additionally, it was noticed that the C=O absorbance peak vanished. The OH groups of GO and AmGO are responsible for the wide band at 3000–3300 cm^{-1} (El-Monaem et al. 2021). The MoO_3 spectrum elucidates a peak at 3306 cm^{-1} belonging to the H–*O*–H bending (Gowtham et al. 2018). The band at 811 and 674 cm^{-1} is assigned to Mo–O–Mo and Mo–O, respectively, while the related band to Mo=O is located at 855 cm^{-1} (Gowtham et al. 2018). The bands at 641, 594, and 545 cm^{-1} are attributed to the oxygen-containing atoms in MoO_3 [26]. The C–O and C–N of *A. halimus* emerged at 1108 and 1197 cm^{-1}, respectively (Abdelfatah et al. 2022). For the ZIF-67 spectrum, the bands ranging from 600 to 1500 cm^{-1} are assigned to the imidazole ring bending and stretching modes. The stretching mode of C=N appeared at 1569 cm^{-1}, and the C–H stretching in the aliphatic chain and aromatic ring manifested at 2920 and 3180 cm^{-1} (Tang et al. 2018). The peak at 424 cm^{-1} belongs to Co–N in ZIF-67 (Zhang et al. 2021). The MoO_3/ZIF-67/AmGO spectrum represents the distinctive peaks of ZIF-67, MoO_3, and AmGO, implying a well combination between these components.

XRD

The XRD patterns of GO, AmGO, MoO_3, ZIF67, and MoO_3/ZIF67/AmGO are provided in Fig. 2B. The GO pattern illustrates its distinctive XRD peak located at 10.25°, whereas the AmGO pattern discloses three peaks at 10.33°, 26.17°, and 42.71°, denotes occurring the amination process of GO (Bin Wang et al. 2011). The orthorhombic structure of MoO_3 NPs was inferred by the appearance of the distinguishing XRD peaks at 12.75°, 23.45°, 25.70°, 28.11°, 33.35°, 38.21°, and 45.59°, which attributed to the (020), (110), (040), (021), (111), (060), and (200) planes, respectively (Eltaweil et al. 2022). The existence of ZIF-67 distinctive peaks in XRD patterns at 7.80°, 10.41°, 2.75°, 15.51°, 17.06°, 18.04°, 21.78°, 23.42°, 27.7°, and 29.09° demonstrates its well-fabrication with no impurities (Shahsavari et al. 2022). The XRD pattern of the MoO_3/ZIF67/AmGO composite shows a noticeable diminution in the intensities of the belonging peaks to MoO_3 and ZIF-67, with a disappearance of some peaks. This observation owes to the amorphous nature of AmGO, and it implied the composite formation.

XPS

According to the XPS survey (Fig. 3A), MoO_3/ZIF-67/AmGO composes of Mo3d, C1s, O1s, N1s, and Co2p. The two distinct peaks of the Mo3d spectrum belong to the Mo^{+6}3d5/2 and Mo^{+6}3d3/2, respectively (Fig. 3B). There are three carbon peaks; C–O, O–C=O, and C–C manifested at 285.26, 291.59, and 284.57 eV, respectively (Fig. 3C) (Alharthi et al. 2023). The O1s spectrum (Fig. 3D) elucidates Mo–O in the α-MoO_3 lattice and C=O bands at 530.3 and 531.3 eV (Li et al. 2020; Thomas et al. 2021). The N1s peak that appeared at 398.8 eV belongs

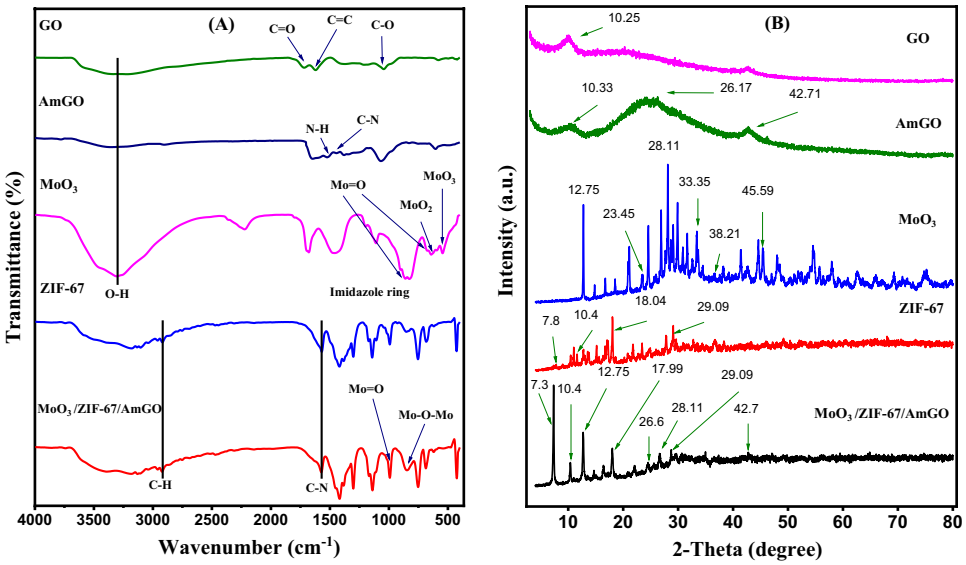

Fig. 2 **A** FTIR and **B** XRD of GO, AmGO, MoO_3, ZIF-67and MoO_3/ZIF-67/AmGO

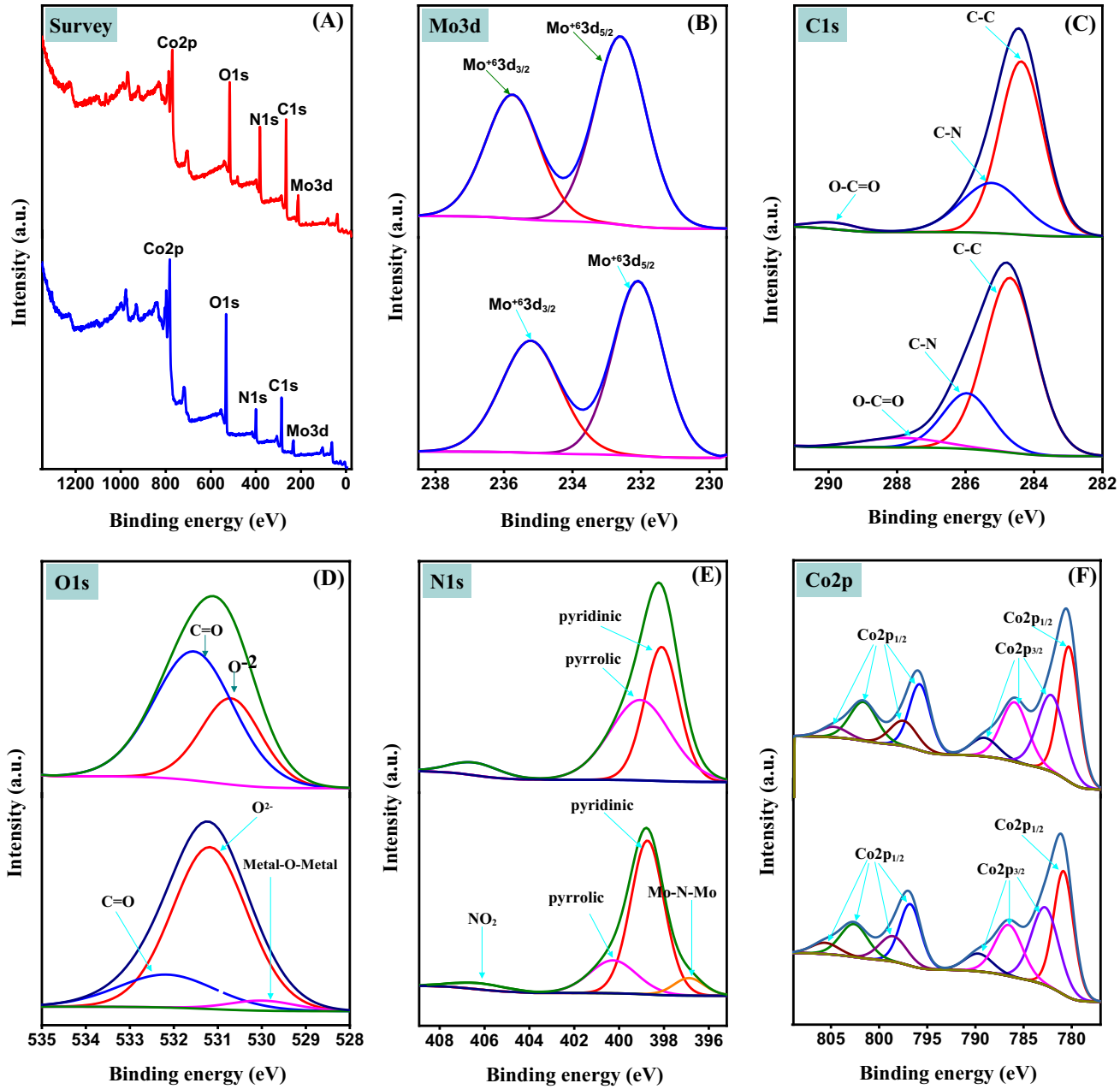

Fig. 3 XPS spectra of MoO_3/ZIF-67/AmGO before and after *o*-NP adsorption. **A** Survey, **B** Mo3d, **C** C1s, **D** O1s, **E** N1s, and **F** Co2p

to Co–N, while the peak at 399.0 eV corresponds to N–H (Shin et al. 2023; Vinoth et al. 2017), and the peak at 406.6 eV is assigned to N-graphitic (Fig. 3E) (Almheiri et al. 2019). The Co spectrum revealed the Co^{2+} peaks at 782.72 and 798.3 eV for Co^{2+}2p3/2 and Co^{2+}2p1/2, subsequently, with the appearance of their satellite peaks at 789.7 and 805.7 eV (Fig. 3F). In addition, the Co^{2+} peaks at 780.85 eV for Co^{2+}2p3/2, and 796.68 eV for Co^{2+}2p1/2, along with their satellite peaks at 786.59 and 802.6 eV (Kitchamsetti et al. 2020).

SEM

The morphology of the pristine *A.halimus biomass* and the fabricated samples were investigated using SEM (Fig. 4). The SEM of *Atriplex halimus* shows a nonporous creased cellular morphology, while the SEM of plant-derived BC displays a flake-like structure. This morphology change is most likely due to the thermal degradation of chemical bonds at high pyrolysis temperatures during BC synthesis (Zhang et al. 2009). The SEM of the green-synthesized

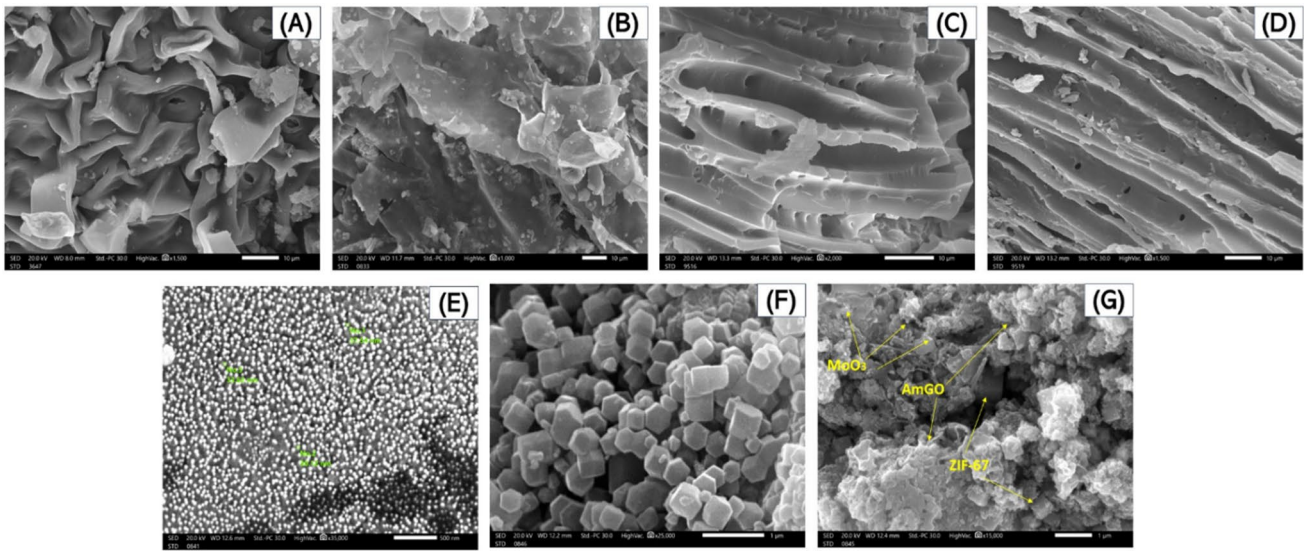

Fig. 4 SEM images of **A** *A. halimus biomass*, **B** *A. halimus*-derived BC, **C** GO, **D** AmGO, **E** MoO_3, **F** ZIF-67, and **G** MoO_3/ZIF-67/AmGO composite

GO elucidated a porous channel-like structure. The AmGO image revealed that the walls of the channel-like structure of GO became thinner with the appearance of some fractures on the surface, which corresponds to the incorporation of the amine group into GO. Furthermore, the SEM image for the green MoO_3NPs demonstrates the orthorhombic structure with an approximated average particle size between 30 and 37 nm. The SEM image of ZIF-67 exhibits a rhombohedral dodecahedron crystal morphology. The SEM images of the MoO_3/ZIF-67/AmGO composite display the successful formation of ZIF-67 and MoO_3NPs crystals onto the AmGO.

Zeta potential measurements

The surface charge of the MoO_3/ZIF-67/AmGO composite was investigated using zeta potential, denoting that the pH_{PZC} was 6.4 (Fig. 5A). Hence, the net surface charge of MoO_3/ZIF-67/AmGO over pH 6.4 is negative, reflecting the favorability of the composite to adsorb cationic contaminants in an alkaline medium. Conversely, MoO_3/ZIF-67/AmGO carried is rich with positive charges at pH below 6.4. So, the composite possesses a superb aptitude to adsorb anionic pollutants. Notably, the pH_{PZC} is near 7, suggesting the zwitter character to MoO_3/ZIF-67/AmGO, giving merit to the composite that could adsorb the zwitter contaminants.

Optimization of the *o*-NP adsorption process

Comparison test

A comparison test proceeded between the three fabricated MoO_3/ZIF-67/AmGO composites and the authentic components to demonstrate the synergistic effect between these green components to boost the *o*-NP adsorption percentage (Fig. 5B). The removal efficiency of MoO_3, ZIF-67, and AmGO were 59.55, 61.79, and 55.05%, and their adsorption capacities were 119.10, 123.59, and 199.98 mg/g, respectively. Moreover, the removal aptitude of the composites with varied MoO_3: AmGO ratios (viz., 2:1, 1:1, and 1:2) toward *o*-NP was studied. The R% and the q of MoO_3/ZIF-67/AmGO composite with MoO_3: AmGO ratio 2:1 were 79.77% and 159.55 mg/g, while in the case of 1:1 ratio R% and q were 67.41% and 134.83 mg/g, and for ratio 1:2, R = 71.91% and q = 143.82 mg/g, respectively. Based on these results, the MoO_3/ZIF-67/AmGO composite with MoO_3: AmGO ratios of 2:1 provided an enhanced adsorption% of *o*-NP, so it was opted for the rest of the batch study.

The influence of pH

In general, pH is a critical parameter that drastically impacts the adsorption aptitude inside the *o*-NP/MoO_3/ZIF-67/AmGO adsorption system. The pH influence on the *o*-NP uptake onto MoO_3/ZIF-67/AmGO composite was tested at wide pH ranges, as represented in Fig. 5C. The experimental findings implied that *o*-NP superior uptake onto MoO_3/ZIF-67/AmGO was at pH 7. This observation can be attributed to the fact that the pKa of *o*-NP is 7.23 denotes that *o*-NP remains in the molecule form in the acidic and natural media (Liptak et al. 2002). Accordingly, there is no substantial electrostatic repulsion force exists between *o*-NP and MoO_3/ZIF-67/AmGO that could affect the adsorption process. Therefore, the *o*-NP adsorption onto MoO_3/ZIF-67/AmGO depends on other physical and chemical interactions, such

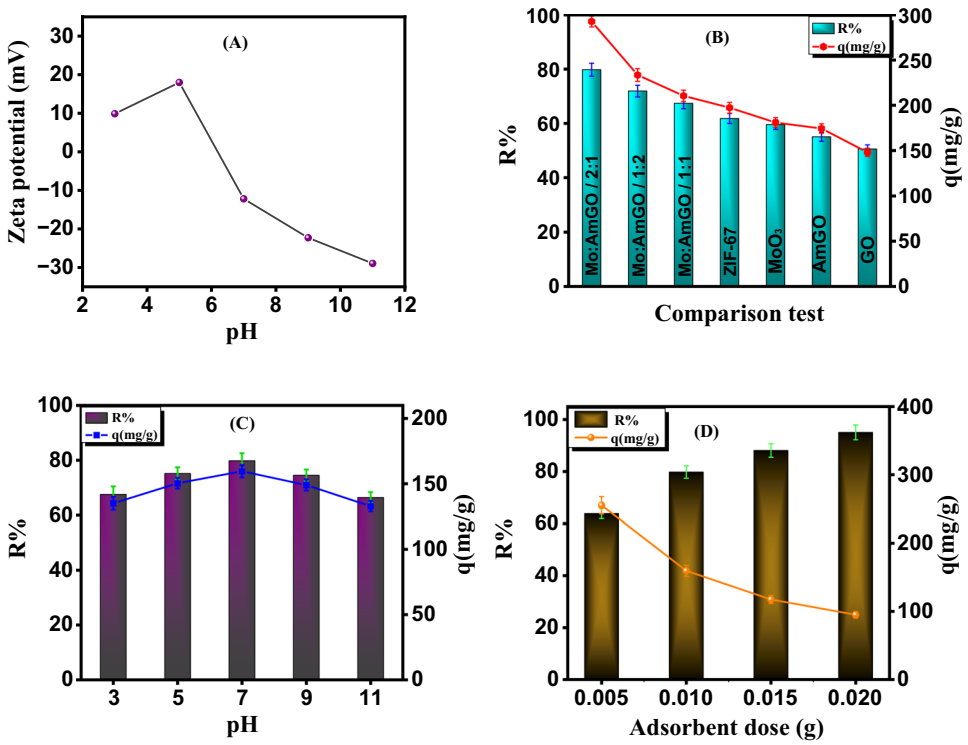

Fig. 5 **A** Zeta potential of MoO_3/ZIF-67/AmGO composite, **B** Comparison study [pH = 6, T = 25 °C, m = 0.01 g, and C_o = 100 mg/L], **C** the effect of pH [pH = 3–11, T = 25 °C, m = 0.01 g, and, C_o = 50 mg/L], and **D** the effect of the MoO_3/ZIF-67/AmGO dose [m = 0.005–0.02 g, T = 25 °C, pH = 6, and C_o = 100 mg/L] on the adsorption of *o-NP*

as H-bonding, π–π interaction, and electron donor–acceptor interaction. On the contrary, the R% and q of MoO_3/ZIF-67/AmGO decrease as pH values increase over pH = 7. Such a diminution in the *o*-NP adsorption efficacy owes to the strong electrostatic repulsion forces between the anionic *o*-NP molecules and the anionic adsorption sites on the MoO_3/ZIF-67/AmGO surface (Abd El-Monaem et al. 2023b).

The influence of the MoO_3/ZIF-67/AmGO dose

The MoO_3/ZIF-67/AmGO amount drastically influences the efficacy of adsorbing *o*-NP; therefore, the *o*-NP adsorption aptitude was examined using different amounts of MoO_3/ZIF-67/AmGO (Fig. 5D). The results depicted that the R% of *o*-NP boosted from 63.82% using 0.005 g of the composite to 95.05% when the dose elevated to 0.02 g. This enhancement in the *o*-NP removal efficacy owes to the increase in the active sites that participate in the adsorption process. On the contrary, the capacity of the adsorbed *o*-NP molecules dwindled from 255.28 to 95.05 mg/g, which may be attributed to the aggregation of the over amounts of composite, causing a decline in the surface area.

The influence of the initial *o*-NP concentration

The concentration influence on the efficacy of the *o*-NP adsorption onto MoO_3/ZIF67/AmGO was inspected at concentrations ranging from 50 to 300 mg/L. The adsorption capacity of MoO_3/ZIF-67/AmGO toward *o*-NP increased from 91.46 to 397.87 mg/g when raising the concentration from 50 to 300 mg/L (Fig. 6A). This increase could be due to the high *o*-NP driving force, outdoing the *o*-NP transfer resistance that prevents the particles' migration to MoO_3/ZIF-67/AmGO composite (Eltaweil et al. 2023). On the contrary, the efficiency of the *o*-NP removal decreased from 92.47 to 53.36%, which may be ascribed to the inadequacy in the adsorption groups of the MoO_3/ZIF67/AmGO composite (Fig. 6B) (Omer et al. 2022).

The influence of the system temperature

The influence of temperature on the thermodynamic nature of the MoO_3/ZIF-67/AmGO/*o*-NP system was scrutinized (Fig. 6C). The acquired result revealed the endothermal adsorption nature of the MoO_3/ZIF-67/AmGO~*o*-NP system since q and R% increased from 159.15 mg/g and 79.77% to 180.22 mg/g and 90.11% with elevating the system temperature from 25 to 55 °C, respectively. Such an amelioration in the *o*-NP removal efficacy is most probably due to the increased Brownian motion of *o*-NP at higher temperatures, which facilitates the adsorption process.

Isotherm study

An isotherm study was performed using Langmuir, Freundlich, Temkin, and Dubinin-Radushkevich to define the interaction nature inside the MoO_3/ZIF-67/AmGO/*o*-NP system at equilibrium (Fig. 7A–D). Langmuir isotherm

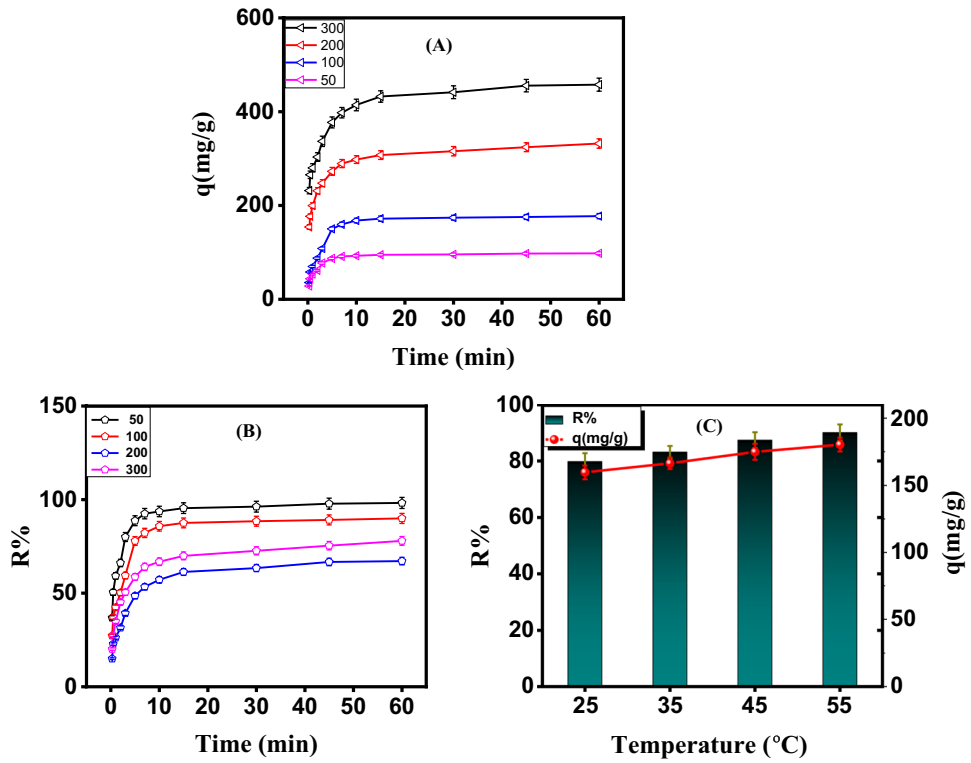

Fig. 6 **A**, **B** impact of *o*-NP initial concentration [C_o = 50–200 mg/L, T = 25 °C, pH = 6, and m = 0.01 g] on *o*-NP adsorption onto MoO_3/ZIF67/AmGO composite **C** impact of temperature [T = 25–55 °C, pH = 6, C_o = 50 mg/L, and m = 0.01 g] on *o-NP* adsorption onto MoO_3/ZIF67/AmGO composite

assumes a monolayer adsorption process and that the adsorbent has a homogeneous surface in which all active sites require the same adsorption energy without interaction between adsorbed molecules (Cheng et al. 2022). Freundlich isotherm assumes a multi-layer adsorption process accompanied by physical interaction between adsorbed molecules. Freundlich assumes that adsorbent has a heterogeneous surface with various kinds of active sites (Patel and Hota 2016).

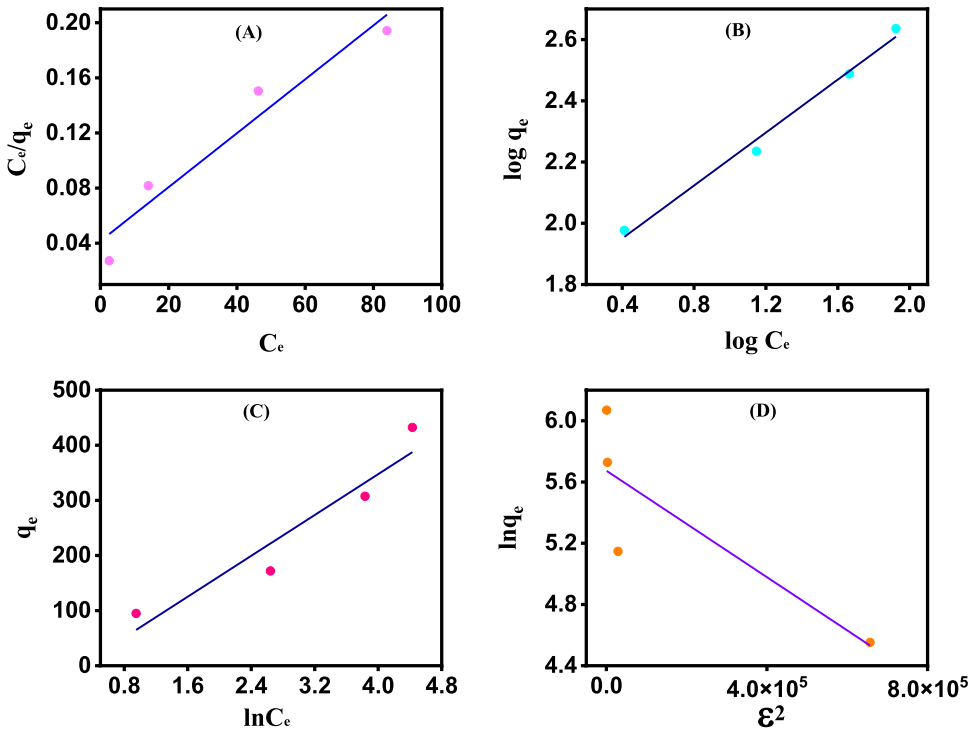

Fig. 7 Isotherm model for *o*-NP adsorption onto MoO_3/ZIF-67/AmGO. **A** Langmuir, **B** Freundlich, **C** Temkin models, and **D** Dubinin-Radushkevich

According to the Temkin isotherm, adsorption is a multilayer process that takes into account interactions between the adsorbent and the adsorbate (Qin et al. 2023a). The adsorption process on both homogeneous and heterogeneous surfaces may also be explained by the Dubinin-Radushkevich isotherm (Cheng et al. 2023). Table S1 summarizes the linear equations of the isotherms. The correlation coefficient, R^2, is used as an index to assess the suitability of the isotherm models. The computed isotherm parameters demonstrated that Freundlich has a higher R^2 (0.98) value compared to that of the other three models as depicted in Table 1. This demonstrated the suitability of Freundlich to exemplify the uptake of *o*-NP onto MoO_3/ZIF-67/AmGO, indicating the occurrence of the physisorption of *o*-NP onto the composite surface. The *n* value of Freundlich displays the suitability of MoO_3/ZIF-67/AmGO to adsorb *o*-NP since it is larger than two. Based on Langmuir the q_{max} of *o*-NP onto MoO_3/ZIF-67/AmGO composite attained 500 mg/g, reflecting the superior capacity of MoO_3/ZIF-67/AmGO to adsorb such phenolic compounds. The b value from the Temkin suggests that the adsorption of *o*-NP was via physisorption since it is lower than 80 kJ/mol. Also, the E value of D-R implied proceeding physical interactions between *o*-NP and MoO_3/ZIF-67/AmGO.

Kinetic study

A kinetic study (Fig. 8A–C) was conducted on the acquired adsorption data to determine the rate and nature of *o*-NP adsorption onto MoO_3/ZIF-67/AmGO, whether it occurred by chemical or physical interactions. The Pseudo-1st-order assumes that the adsorption process is governed by physical interactions, whereas the Pseud*o* 2nd order supposed that chemical interactions are the controlling forces on the adsorption process (Ledesma et al. 2023). Elovich model is used to describe the chemisorption process and is applied to heterogenous surface adsorbents (Edet and Ifelebuegu 2020). Table S2 lists the linear kinetic expressions of Pseudo-1st-order, Pseudo-2nd-order, and Elovich. The computed kinetic parameters are listed in Table 2. The kinetic analysis results demonstrated that the Pseudo-2nd-order model has a higher R^2 compared to the other two models. Additionally, the calculated values ($q_{e,cal}$) of the Pseudo-2nd-order are closer to experimental values ($q_{e,exp}$) at the different concentrations of 50–300 mg/L. The Pseudo-2nd-order is therefore better describing the *o*-NP adsorption onto MoO_3/ZIF-67/AmGO, depicting that chemisorption is the key step in governing the adsorption rate. Moreover, the rate constant values of Pseudo-2nd-order (k_2) decreased as initial *o*-NP concentrations (50–300 mg/L) increased. This observation also emphasizes that chemisorption is the rate-limiting step in the adsorption process. The initial adsorption constant (h) of *o*-NP is higher than the rate constant (k_2) at concentrations of 50–300 mg/L. These results indicate that the *o*-NP adsorption rate is faster at the beginning of the adsorption process, then consistently decreases with increasing adsorption time. Moreover, the Elovich model shows a high adsorption affinity of *o*-NP onto MoO_3/ZIF-67/AmGO since the *o*-NP adsorption rate (α) is much higher than the desorption rate (β).

Table 1 Isotherm model parameters derived from Langmuir, Freundlich, Temkin, and Dubinin-Radushkevich for the adsorption of *o*-NP onto MoO_3/ZIF-67/AmGO composite

Isotherm models and parameters	
Langmuir	
q_{max}(mg/g)	500
K_L (L/mg)	0.048
R^2	0.93
Freundlich	
k_f (L/mg)	59.89
n	2.035
R^2	0.98
Temkin	
K_T(L/g)	1.28
B (J/mol)	92.68
b (KJ/mol)	0.26
R^2	0.90
D-R	
K_{DR}	2×10^{-6}
E (KJ/mol)	0.500
R^2	0.70

Thermodynamics study

The thermodynamic nature of the MoO_3/ZIF-67/AmGO/*o*-NP system was scrutinized using can't Hoff curve (Fig. 9A). Text S3 explained the thermodynamic expressions. The reckoned positive ΔS° reflected the randomness of the *o*-NP molecule's adsorption on the MoO_3/ZIF-67/AmGO surface (Table 3). The derived positive ΔH° inferred that the *o*-NP adsorption onto MoO_3/ZIF-67/AmGO is endothermic. Furthermore, the spontaneity of the *o*-NP uptake was indicated by the computed negative ΔG° values at different system temperatures. It is observed that with increasing adsorption temperature the values of ΔG° decrease. This indicates that the *o*-NP adsorption on the MoO_3/ZIF-67/AmGO is facile at high adsorption temperatures. This finding is valuable in the real implementation process.

Adsorption mechanism

The promising aptitude of MoO_3/ZIF-67/AmGO during the removal process of *o*-NP from an aqueous medium, rendering the investigation of the adsorption mechanism is a significant point to denote the plenteous adsorption

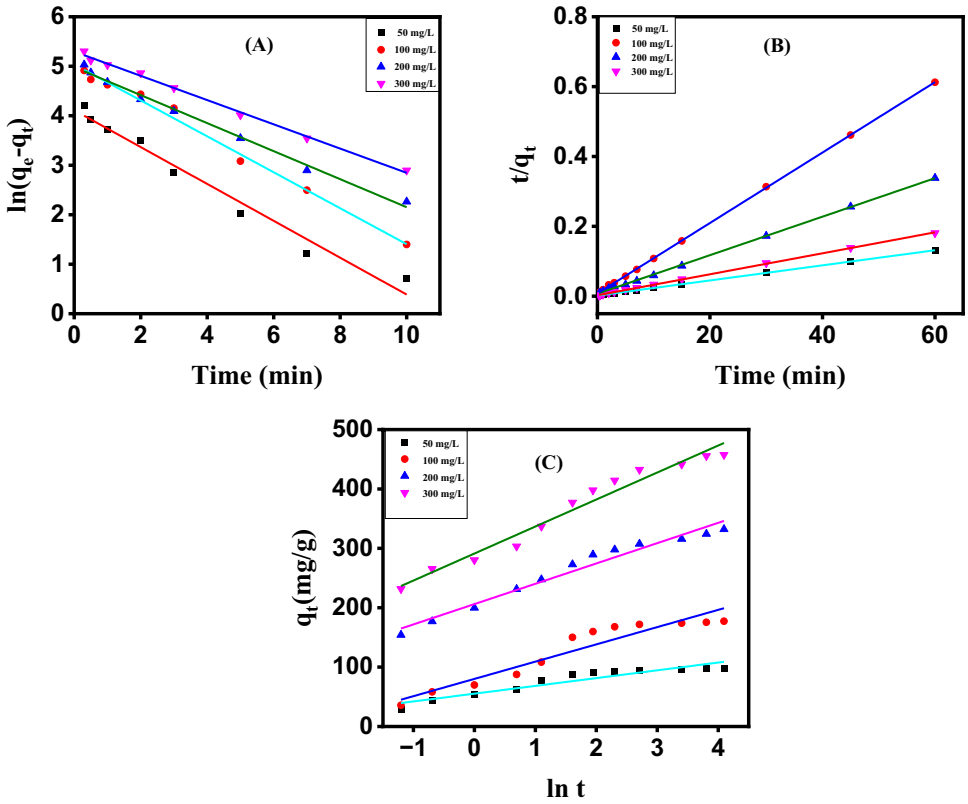

Fig. 8 Kinetic model for *o*-NP adsorption onto MoO_3/ZIF-67/AmGO. **A** Pseudo-1st-order, **B** Pseudo-2nd-order, and **C** Elovich models

Table 2 Kinetic model parameters derived from Pseudo-1st-order, Pseudo-2nd-order, and Elovich for the adsorption of *o*-NP onto MoO_3/ZIF-67/AmGO composite

Kinetic models and parameters				
Concentration (mg/L)	50	100	200	300
$q_{e,exp}$ (mg/g)	94.83	171.91	307.49	432.40
PFO				
$q_{e,cal}$ (mg/g)	50.02	145.69	161.25	161.25
k_1 (min^{-1})	0.29	0.34	0.320	0.327
R^2	0.94	0.99	0.98	0.95
PSO				
$q_{e,cal}$ (mg/g)	99.009	181.81	333.33	454.54
K_2 (g/mg.min)	0.0127	0.0041	0.0033	0.0025
h ($mg/g.min^{-1}$)	124.49	135.52	366.65	516.51
R^2	0.99	0.99	0.99	0.99
Elovich				
α (mg/g.min)	890.50	457.49	14,146.85	27,412.82
β (g/mg)	0.076	0.034	0.029	0.021
R^2	0.89	0.90	0.96	0.96

sites-containing green-fabricated composite and their abilities to grasp the *o*-NP molecules from wastewater. Firstly, the kinetic investigation implied the *o*-NP chemisorption onto MoO_3/ZIF-67/AmGO, while the isotherm study clarified the presence of physical interactions inside the MoO_3/ZIF-67/AmGO/*o*-NP system. Secondly, characterization analyses (XPS, ZP, and FTIR) were applied to identify the interactions between MoO_3/ZIF-67/AmGO and *o*-NP during the studied adsorption process. For FTIR, by comparing the authentic MoO_3/ZIF-67/AmGO with the used one, it was noticed manifesting a peak at 1502 cm^{-1}, which belongs to N=O of *o*-NP, which infers occurrence of the *o*-NP adsorption onto the green composite (Fig. 9B). In addition, significant diminution in the peaks' intensity with a redshift, reflecting the contribution of the active adsorption groups of MoO_3/ZIF-67/AmGO in adsorbing *o*-NP. For ZP, it was evinced the negative influence of the electrostatic interaction for the existence of *o*-NP in a molecular form at pH < 7.23, while it becomes an anionic molecule when pH exceeds 7.23. Meanwhile, MoO_3/ZIF-67/AmGO carried negative charges in the alkaline medium, thus repulsion forces generated in the MoO_3/ZIF-67/AmGO/*o*-NP system, resulting in a diminution in the removal efficacy of *o*-NP.

For XPS, the shifting of the belonging peaks to Co2p (Fig. 3F) and Mo3d (Fig. 3B) may be attributed to the coordination bonds formation between the metal species of MoO_3/ZIF-67/AmGO and the oxygenated functional groups of *o*-NP. Furthermore, the possibility of occurring e-donner/acceptor interaction between MoO_3/ZIF-67/AmGO and *o*-NP, where benzene ring, OH, and NH_2 (e-donner groups) of MoO_3/ZIF-67/AmGO could endow electrons to nitro group (e-acceptor group) of *o*-NP. Additionally, the

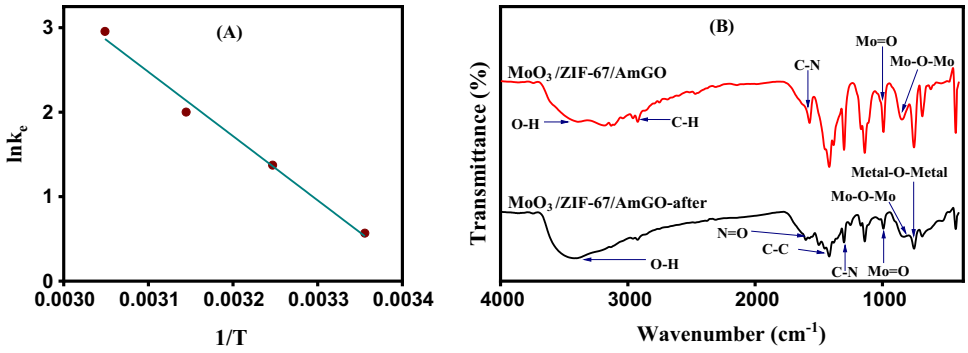

Fig. 9 **A** van't Hoff plot for *o*-NP adsorption onto MoO_3/ZIF-67/AmGO composite, and **B** FTIR of MoO_3/ZIF-67/AmGO before and after *o*-NP adsorption

Table 3 Thermodynamic parameters for the adsorption of *o*-NP onto MoO_3/ZIF-67/AmGO composite

Thermodynamics parameters				
Temperature (K)	ΔH (KJ/mol)	ΔS (J/mol·K)	ΔG (KJ/mol)	R^2
298	63.23	216.60	− 1.31	0.99
308			− 3.48	
318			− 5.64	
328			− 7.81	

e-acceptor groups of MoO_3/ZIF-67/AmGO (COOH) could chelate electrons from the e-donner groups of *o*-NP (aromatic ring and OH). This suggestion was assured by the noticeable shift in the XPS peak position of both O1s and N1s spectra (Fig. 3D, E). Moreover, H-bonding is another pathway to adsorb *o*-NP onto MoO_3/ZIF-67/AmGO via the formed bonds between H-containing in MoO_3/ZIF-67/AmGO and N- and O- of *o*-NP and vice versa. Besides, the aromatic rings in *o*-NP and MoO_3/ZIF-67/AmGO contribute to the *o*-NP adsorption by forming π–π interaction.

To sum up, the green MoO_3/ZIF-67/AmGO composite could adsorb *o*-NP onto its surface via bountiful pathways, comprising π–π interaction, e-donner/acceptor interaction, coordination bond, and H-bonding (Fig. 10). Conversely, electrostatic repulsion exhibited a negative influence on the adsorption process inside the MoO_3/ZIF-67/AmGO/*o*-NP system.

Removal of *o*-NP from real wastewater

Samples of actual wastewater were collected from the industrial discharge of a paint manufacturing in Alexandria, Egypt. The removal aptitude of *o*-NP by MoO_3/ZIF-67/AmGO composite was evaluated as follows: soaking 0.01g of MoO3/ZIF-67/AmGO into 20 mL of the *o*-NP-containing actual wastewater. Table S3 lists wastewater characteristics before and after adsorption. The calibration curve showed that the *o*-NP concentration in the collected samples was about 55.4 mg/L. Although the composition of the actual wastewater is more complex than laboratory-prepared synthetic solutions, *o*-NP rapidly adsorbed in the first 7 min of the adsorption process and slowly eliminated till 60 min (Fig. S1). With the increase in contact time, the efficiency of the *o*-NP removal increased from 83.65 to 89.29%, and the adsorption capacity increased from 98.65 to 105.25 mg/g, confirming the applicability of MoO_3/ZIF-67/AmGO composite for *o*-NP removal from actual wastewater.

The effect of ionic strength

The ionic strength test was conducted using different concentrations of NaCl, as elucidated in Fig. 11A. A remarkable improvement in the R% of *o*-NP (65.28–71.79%) and the q 130.56–143.59 mg/g) was observed by increasing the NaCl concentration from 0.2 to 1.0 Mol/L. This performance owes to the salting-out effect that could be explained by the disordering of the H_2O molecules in the existence of dissolved ions, declining the available cavities to accommodate *o*-NP. Thus, the solubility of *o*-NP diminishes, and the adsorbability of the molecules directly increases (Tang et al. 2007).

Reusability study

Figure 11B elucidates the superior recyclability of the green-fabricated MoO_3/ZIF-67/AmGO composite, where it conserved its high capacity toward the *o*-NP adsorption (128.09 mg/g) after five cycles. This promising performance reflected the viability of the green-fabricated composite, which provides superb adsorption capacity, propitious recyclability, and super-fast adsorption, in addition to the eco-friendly and low capital cost features.

Conclusion

In this research, a sustainable and renewable resource, *A.halimus*, was opted to synthesize MoO3/ZIF-67/AmGO composite for the first time. The ZP analysis demonstrated

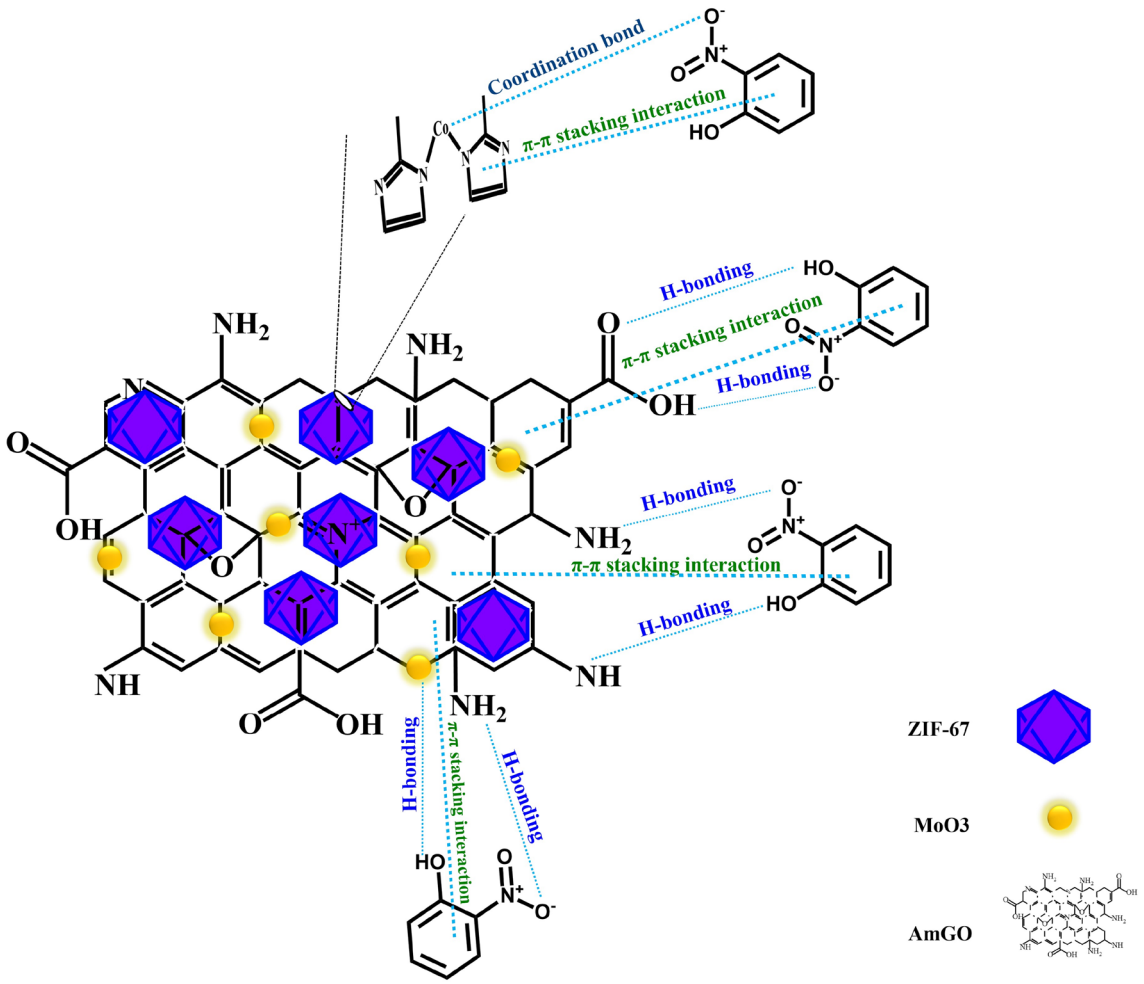

Fig. 10 Possible mechanism for *o*-NP adsorption onto MoO_3/ZIF-67/AmGO composite

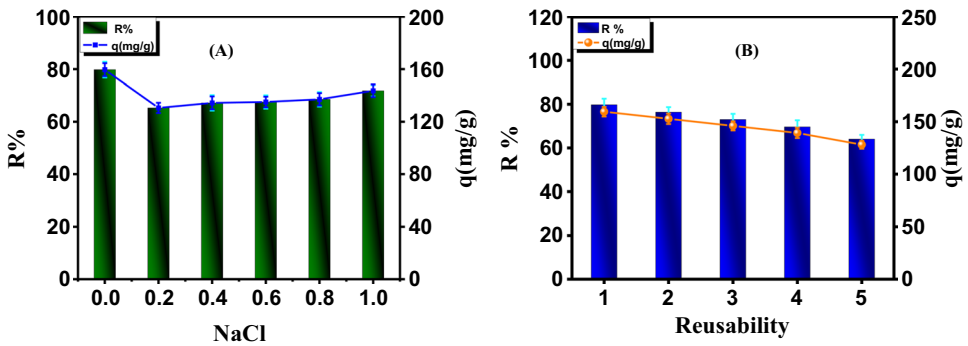

Fig. 11 **A** effect of ionic strength [NaCl concentration = 0.2–1.0 mol/L, T = 25 °C, pH = 6, C_o = 50 mg/L, and m = 0.01 g] on *o*-NP adsorption onto MoO_3/ZIF67/AmGO composite, **B** reusability study [NaOH concentration = 1 M, T = 25 °C, pH = 6, m = 0.01 g, and C_o = 50 mg/L]

that the pH_{PZC} of MoO_3/ZIF-67/AmGO was 6.4. FTIR, XRD, and SEM ensured the complete combination between MoO_3, ZIF-67, and AmGO to produce a composite. The data obtained from the adsorption experiment approved the quick (10 min) and higher aptitude of *o*-NP adsorption at pH 7, using 0.01 g of MoO_3/ZIF-67/AmGO. The recyclability test reveals that MoO_3/ZIF-67/AmGO composite can be used for up to five cycles with high adsorption potential, 128.09 mg/g. The isotherms and kinetics elucidated that the *o*-NP adsorption onto MoO_3/ZIF-67/AmGO fitted the Freundlich and Pseudo-2nd-order, subsequently. The proposed mechanism for *o*-NP adsorption is designated by π–π interaction, e-donner/acceptor interaction, coordination bond, and H-bonding. Additionally, data from FTIR and XPS add more support to the assumed pathway. The high adsorption efficacy, recyclability, and green nature of MoO_3/ZIF67/

AmGO composite make it an ec*o*-friendly, and sustainable candidate for the remediation of toxic organic pollutants from wastewater.

Supplementary Information The online version contains supplementary material available at https://doi.org/10.1007/s13201-024-02194-3.

Acknowledgements The authors acknowledge the financial support obtained from The Egyptian Science, Technology & Innovation Funding Authority (STDF).

Funding Open access funding provided by The Science, Technology & Innovation Funding Authority (STDF) in cooperation with The Egyptian Knowledge Bank (EKB). Chemicals purchases, glassware, and basic laboratory instruments used in the experimental part were only supported by The Egyptian Science, Technology & Innovation Funding Authority (STDF), grant number 45888 under the umbrella of USAID/STDF collaborative project.

Declarations

Conflict of interest The authors declare that they have no known competing financial interests or personal relationships that could have appeared to influence the work reported in this paper.

Open Access This article is licensed under a Creative Commons Attribution 4.0 International License, which permits use, sharing, adaptation, distribution and reproduction in any medium or format, as long as you give appropriate credit to the original author(s) and the source, provide a link to the Creative Commons licence, and indicate if changes were made. The images or other third party material in this article are included in the article's Creative Commons licence, unless indicated otherwise in a credit line to the material. If material is not included in the article's Creative Commons licence and your intended use is not permitted by statutory regulation or exceeds the permitted use, you will need to obtain permission directly from the copyright holder. To view a copy of this licence, visit http://creativecommons.org/licenses/by/4.0/.

References

Aazza M, Ahlafi H, Moussout H, Maghat H (2017) Ortho-Nitro-Phenol adsorption onto alumina and surfactant modified alumina: kinetic, isotherm and mechanism. J Environ Chem Eng 5(4):3418–3428. https://doi.org/10.1016/j.jece.2017.06.051

Abd El-Monaem EM, Ayoup MS, Omer AM, Hammad EN, Eltaweil AS (2023a) Sandwich-like construction of a new aminated chitosan Schiff base for efficient removal of Congo red. Appl Water Sci 13(2):67

Abd El-Monaem EM, Elshishini HM, Bakr SS, El-Aqapa HG, Hosny M, Andaluri G, El-Subruiti GM, Omer AM, Eltaweil AS (2023) A comprehensive review on LDH-based catalysts to activate persulfates for the degradation of organic pollutants. npj Clean Water 6(1):34. https://doi.org/10.1038/s41545-023-00245-x

Abd El-Monaem EM, Eltaweil AS, El-Subruiti GM, Mohy-Eldin MS, Omer AM (2023) Adsorption of nitrophenol onto a novel Fe_3O_4-κ-carrageenan/MIL-125 (Ti) composite: process optimization, isotherms, kinetics, and mechanism. Environ Sci Pollut Res. https://doi.org/10.1007/s11356-023-25678-2

Abdelfatah AM, El-Maghrabi N, Mahmoud AED, Fawzy M (2022) Synergetic effect of green synthesized reduced graphene oxide and nano-zero valent iron composite for the removal of doxycycline antibiotic from water. Sci Rep 12(1):19372

Alharthi FA, Alshammari RH, Hasan I (2023) Synthesis of Xanthan Gum anchored α-Fe_2O_3 bionanocomposite material for remediation of Pb (II) contaminated aquatic system. Polymers 15(5):1134

Almheiri S, Ahmad AA, Le Droumaguet B, Pires R, Mohamed AA, Chehimi MM (2019) Development of latent fingerprints via aryldiazonium tetrachloroaurate salts on copper surfaces: an XPS study. Langmuir 36(1):74–83

Bestawy EE, El-Shatby BF, Eltaweil AS (2020) Integration between bacterial consortium and magnetite (Fe_3O_4) nanoparticles for the treatment of oily industrial wastewater. World J Microbiol Biotechnol 36:1–16

Chen J, Sun X, Lin L, Dong X, He Y (2017) Adsorption removal of o-nitrophenol and p-nitrophenol from wastewater by metal–organic framework Cr-BDC. Chin J Chem Eng 25(6):775–781. https://doi.org/10.1016/j.cjche.2016.10.014

Cheng N, Ren L, Xu X, Du Y, Dou SX (2018) Recent development of zeolitic imidazolate frameworks (ZIFs) derived porous carbon based materials as electrocatalysts. Adv Energy Mater 8(25):1801257

Cheng S, Zhao S, Xing B, Shi C, Meng W, Zhang C, Bo Z (2022) Facile one-pot green synthesis of magnetic separation photocatalyst-adsorbent and its application. J Water Process Eng 47:102802. https://doi.org/10.1016/j.jwpe.2022.102802

Cheng S, Meng W, Xing B, Shi C, Wang Q, Xia D, Nie Y, Yi G, Zhang C, Xia H (2023) Efficient removal of heavy metals from aqueous solutions by Mg/Fe bimetallic oxide-modified biochar: experiments and DFT investigations. J Clean Prod 403:136821. https://doi.org/10.1016/j.jclepro.2023.136821

Cui W, Kang X, Zhang X, Zheng Z, Cui X (2019) Facile synthesis of porous cubic microstructure of Co_3O_4 from ZIF-67 pyrolysis and its Au doped structure for enhanced acetone gas-sensing. Phys E 113:165–171. https://doi.org/10.1016/j.physe.2019.04.026

Dayana Priyadharshini S, Manikandan S, Kiruthiga R, Rednam U, Babu PS, Subbaiya R, Karmegam N, Kim W, Govarthanan M (2022) Graphene oxide-based nanomaterials for the treatment of pollutants in the aquatic environment: recent trends and perspectives—a review. Environ Pollut 306:119377. https://doi.org/10.1016/j.envpol.2022.119377

Demirbas A (2008) Heavy metal adsorption onto agro-based waste materials: a review. J Hazard Mater 157(2):220–229. https://doi.org/10.1016/j.jhazmat.2008.01.024

Edet UA, Ifelebuegu AO (2020) Kinetics, isotherms, and thermodynamic modeling of the adsorption of phosphates from model wastewater using recycled brick waste. Processes. https://doi.org/10.3390/pr8060665

El-Maghrabi N, El-Borady OM, Hosny M, Fawzy M (2021) Catalytic and medical potential of a phyto-functionalized reduced graphene oxide-gold nanocomposite using Willow-Leaved knotgrass. ACS Omega 6(50):34954–34966. https://doi.org/10.1021/acsomega.1c05596

El-Monaem EMA, El-Latif MMA, Eltaweil AS, El-Subruiti GM (2021) Cobalt nanoparticles supported on reduced amine-functionalized graphene oxide for catalytic reduction of nitroanilines and organic dyes. Nano 16(04):2150039

El-Subruiti G, Eltaweil A, Sallam S (2019) Synthesis of active MFe_2O_4/γ-Fe_2O_3 nanocomposites (metal= Ni or Co) for reduction of nitro-containing pollutants and methyl orange degradation. Nano 14(10):1950125

Eltaweil AS, Fawzy M, Hosny M, Abd El-Monaem EM, Tamer TM, Omer AM (2022) Green synthesis of platinum nanoparticles using Atriplex halimus leaves for potential antimicrobial, antioxidant, and catalytic applications. Arab J Chem 15(1):103517. https://doi.org/10.1016/j.arabjc.2021.103517

Eltaweil AS, Abd El-Monaem EM, El-Subruiti GM, Ali BM, Abd El-Latif MM, Omer AM (2023) Graphene oxide incorporated cellulose acetate beads for efficient removal of methylene blue

dye; isotherms, kinetic, mechanism and co-existing ions studies. J Porous Mater 30(2):607–618. https://doi.org/10.1007/s10934-022-01347-6

Ghosh N, Das S, Biswas G, Haldar PK (2022) Review on some metal oxide nanoparticles as effective adsorbent in wastewater treatment. Water Sci Technol 85(12):3370–3395

Gowtham B, Ponnuswamy V, Pradeesh G, Chandrasekaran J, Aradhana D (2018) MoO_3 overview: hexagonal plate-like MoO_3 nanoparticles prepared by precipitation method. J Mater Sci Mater Electron 29:6835–6843

Hanlon D, Backes C, Higgins TM, Hughes M, O'Neill A, King P, McEvoy N, Duesberg GS, Mendoza Sanchez B, Pettersson H (2014) Production of molybdenum trioxide nanosheets by liquid exfoliation and their application in high-performance supercapacitors. Chem Mater 26(4):1751–1763

Hasan IM, Tawfik AR, Assaf FH (2021) Biosynthesis of α-MoO_3 nanoparticles and its adsorption performance of cadmium from aqueous solutions. Adv Nat Sci Nanosci Nanotechnol 12(3):035007

Hosny M, Fawzy M, El-Badry YA, Hussein EE, Eltaweil AS (2022) Plant-assisted synthesis of gold nanoparticles for photocatalytic, anticancer, and antioxidant applications. J Saudi Chem Soc 26(2):101419

Huang H, Wang Y, Zhang Y, Niu Z, Li X (2020) Amino-functionalized graphene oxide for Cr(VI), Cu(II), Pb(II) and Cd(II) removal from industrial wastewater. Open Chem 18(1):97–107

Kitchamsetti N, Choudhary RJ, Phase DM, Devan RS (2020) Structural correlation of a nanoparticle-embedded mesoporous $CoTiO_3$ perovskite for an efficient electrochemical supercapacitor. RSC Adv 10(39):23446–23456. https://doi.org/10.1039/D0RA04052E

Koubaissy B, Joly G, Batonneau-Gener I, Magnoux P (2011) Adsorptive removal of aromatic compounds present in wastewater by using dealuminated faujasite zeolite. Ind Eng Chem Res 50(9):5705–5713

Ledesma B, Sabio E, González-García CM, Román S, Fernandez ME, Bonelli P, Cukierman AL (2023) Batch and continuous column adsorption of p-nitrophenol onto activated carbons with different particle sizes. Processes. https://doi.org/10.3390/pr11072045

Li J, Hou X, Mao Y, Lai C, Yuan X (2020) Enhanced performance of aprotic electrolyte Li–O_2 batteries with SnS_2–SnO_2/C heterostructure as efficient cathode catalyst. Energy Fuels 34(11):14995–15003

Liptak MD, Gross KC, Seybold PG, Feldgus S, Shields GC (2002) Absolute pK_a determinations for substituted phenols. J Am Chem Soc 124(22):6421–6427

Mahmoud AED, El-Maghrabi N, Hosny M, Fawzy M (2022a) Biogenic synthesis of reduced graphene oxide from Ziziphus spina-christi (Christ's thorn jujube) extracts for catalytic, antimicrobial, and antioxidant potentialities. Environ Sci Pollut Res 29(59):89772–89787. https://doi.org/10.1007/s11356-022-21871-x

Mahmoud AED, Hosny M, El-Maghrabi N, Fawzy M (2022b) Facile synthesis of reduced graphene oxide by Tecoma stans extracts for efficient removal of Ni (II) from water: batch experiments and response surface methodology. Sustain Environ Res 32(1):22. https://doi.org/10.1186/s42834-022-00131-0

Masjedi-Arani M, Amiri M, Amiri O, Ahmadi M, Salavati-Niasari M (2020) Glioma cells eradication by photoexcitation of bioengineered molybdenum trioxide nanoparticles synthesized by wet chemical and microwave route: dose dependent photosensitizer bioactivity. Int J Pharm 591:120021

Omer AM, Abd El-Monaem EM, Eltaweil AS (2022) Novel reusable amine-functionalized cellulose acetate beads impregnated aminated graphene oxide for adsorptive removal of hexavalent chromium ions. Int J Biol Macromol 208:925–934

Patel S, Hota G (2016) Iron oxide nanoparticle-immobilized PAN nanofibers: synthesis and adsorption studies. RSC Adv 6(19):15402–15414. https://doi.org/10.1039/C5RA20345G

Patel KD, Singh RK, Kim H-W (2019) Carbon-based nanomaterials as an emerging platform for theranostics. Mater Horiz 6(3):434–469. https://doi.org/10.1039/C8MH00966J

Pauletto PS, Moreno-Pérez J, Hernández-Hernández LE, Bonilla-Petriciolet A, Dotto GL, Salau NPG (2021) Novel biochar and hydrochar for the adsorption of 2-nitrophenol from aqueous solutions: an approach using the PVSDM model. Chemosphere 269:128748. https://doi.org/10.1016/j.chemosphere.2020.128748

Pham T-H, Lee B-K, Kim J (2016) Improved adsorption properties of a nano zeolite adsorbent toward toxic nitrophenols. Process Saf Environ Prot 104:314–322. https://doi.org/10.1016/j.psep.2016.08.018

Piaskowski K, Zarzycki PK (2020) Carbon-based nanomaterials as promising material for wastewater treatment processes. Int J Environ Res Public Health. https://doi.org/10.3390/ijerph17165862

Qin X, Meng W, Cheng S, Xing B, Shi C, Nie Y, Wang Q, Xia H (2023) Efficient removal of heavy metal and antibiotics from wastewater by phosphate-modified hydrochar. Chemosphere 345:140484. https://doi.org/10.1016/j.chemosphere.2023.140484

Qin X, Zeng X, Cheng S, Xing B, Shi C, Yi G, Nie Y, Wang Q, Zhang C, Xia H (2023) Preparation of double functional carbon-based ZnO derived from rape straw for dye wastewater treatment. J Water Process Eng 52:103588. https://doi.org/10.1016/j.jwpe.2023.103588

Rafi M, Samiey B, Cheng C-H (2018) Study of adsorption mechanism of congo red on graphene oxide/PAMAM nanocomposite. Materials 11(4):496

Sellaoui L, Yazidi A, Ali J, Dotto GL, Bonilla-Petriciolet A, Oliveira LFS, Badawi M, Chen Z (2021) Theoretical study and analysis of o-nitrophenol adsorption using layered double hydroxides containing Ca-Al, Ni-Al and Zn-Al. Environ Sci Pollut Res 28(32):44547–44556. https://doi.org/10.1007/s11356-021-13882-x

Severo LS, Thue PS, Lima DR, Didó CA, Vasconcellos MAZ, Armas LEG, Lima EC, Benvenutti EV, de Menezes EW (2023) 3D graphene sponge biomass-derived with high surface area applied as adsorbent for nitrophenols. J Environ Chem Eng 11(3):109924. https://doi.org/10.1016/j.jece.2023.109924

Shahsavari M, Mortazavi M, Tajik S, Sheikhshoaie I, Beitollahi H (2022) Synthesis and characterization of GO/ZIF-67 nanocomposite: investigation of catalytic activity for the determination of epinine in the presence of dobutamine. Micromachines 13(1):88

Shin J, Kang DW, Lim JH, An JM, Kim Y, Kim JH, Ji MS, Park S, Kim D, Lee JY (2023) Wavelength engineerable porous organic polymer photosensitizers with protonation triggered ROS generation. Nat Commun 14(1):1498

Tabana L, Tichapondwa S, Labuschagne F, Chirwa E (2020) Adsorption of phenol from wastewater using calcined magnesium-zinc-aluminium layered double hydroxide clay. Sustainability 12(10):4273

Tang D, Zheng Z, Lin K, Luan J, Zhang J (2007) Adsorption of p-nitrophenol from aqueous solutions onto activated carbon fiber. J Hazard Mater 143(1):49–56. https://doi.org/10.1016/j.jhazmat.2006.08.066

Tang J, Jiang S, Liu Y, Zheng S, Bai L, Guo J, Wang J (2018) Electrochemical determination of dopamine and uric acid using a glassy carbon electrode modified with a composite consisting of a Co(II)-based metalorganic framework (ZIF-67) and graphene oxide. Microchim Acta 185:1–11

Thomas T, Jayababu N, Shruthi J, Mathew A, Cerdán-Pasarán A, Hernández-Magallanes JA, Sanal KC, Reshmi R (2021) Room temperature ammonia sensing of α-MoO_3 nanorods grown on glass substrates. Thin Solid Films 722:138575

Vinoth R, Babu SG, Bharti V, Gupta V, Navaneethan M, Bhat SV, Muthamizhchelvan C, Ramamurthy PC, Sharma C, Aswal DK

(2017) Ruthenium based metallopolymer grafted reduced graphene oxide as a new hybrid solar light harvester in polymer solar cells. Sci Rep 7(1):43133

Walker DJ, Lutts S (2014) The tolerance of *Atriplex Halimus* L. to environmental stresses. Emir J Food Agric 26(12):1081–1090. https://doi.org/10.9755/ejfa.v26i12.19116

Wang B, Luo B, Liang M, Wang A, Wang J, Fang Y, Chang Y, Zhi L (2011) Chemical amination of graphene oxides and their extraordinary properties in the detection of lead ions. Nanoscale 3(12):5059–5066

Wang B, Wei S, Wang Y, Liang Y, Guo L, Xue J, Pan F, Tang A, Chen X, Xu B (2018) Effect of milling time on microstructure and properties of nano-titanium polymer by high-energy ball milling. Appl Surf Sci 434:1248–1256

Wang L, Shi C, Pan L, Zhang X, Zou J-J (2020) Rational design, synthesis, adsorption principles and applications of metal oxide adsorbents: a review. Nanoscale 12(8):4790–4815

Yadav TP, Yadav RM, Singh DP (2012) Mechanical milling: a top down approach for the synthesis of nanomaterials and nanocomposites. Nanosci Nanotechnol 2(3):22–48

Zhang Q, Cheng Y, Fang C, Shi J, Chen J, Han H (2021) Functionalized waste cellulose with metal-organic-frameworks as the adsorbent with adjustable pore size: ultralight, effective, and selective removal of organic dyes. J Solid State Chem 302:122361

Zhang A, Sun L, Fu P, Yang T, Hu S, Wang Y, Xinag J (2009) Effects of pyrolysis temperature on characteristics of porosity in biomass chars. Paper presented at the Energy and Environment Technology, International Conference.

Publisher's Note Springer Nature remains neutral with regard to jurisdictional claims in published maps and institutional affiliations.